

1 **Chlorine isotopic compositions of apatite in Apollo 14 rocks: Evidence for widespread**
2 **vapor-phase metasomatism on the lunar nearside ~4 billion years ago**

3 Nicola J. Potts^{1,2,3*}, Jessica J. Barnes^{1,4}, Romain Tartèse^{1,5}, Ian A. Franchi¹, Mahesh Anand^{1,6}

4 ¹Planetary & Space Science, The Open University, Walton Hall, Milton Keynes, MK7 6AA, UK

5 ²Faculty of Earth & Life Sciences, Vrije Universiteit Amsterdam, De Boelelaan 1085, 1081 HV Amsterdam, NL

6 ³School of GeoSciences, King's Buildings, University of Edinburgh, Edinburgh, EH9 3JW, UK

7 ⁴ARES NASA Johnson Space Center, Houston, TX 77058, USA

8 ⁵School of Earth and Environmental Sciences, University of Manchester, Manchester M13 9PL, UK

9 ⁶Department of Earth Sciences, The Natural History Museum, Cromwell Road, London, SW7 5BD UK

10
11 *Corresponding author: nicola.potts@ed.ac.uk
12

13 **ABSTRACT**

14 Compared to most other planetary materials in the Solar System, some lunar rocks display high
15 $\delta^{37}\text{Cl}$ signatures. Loss of Cl in a H<<Cl environment has been invoked to explain the heavy
16 signatures observed in lunar samples, either during volcanic eruptions onto the lunar surface or
17 during large scale degassing of the lunar magma ocean. To explore the conditions under which
18 Cl isotope fractionation occurred in lunar basaltic melts, five Apollo 14 crystalline samples
19 were selected (14053,19, 14072,13, 14073,9, 14310,171 along with basaltic clast 14321,1482)
20 for *in situ* analysis of Cl isotopes using secondary ion mass spectrometry. Cl isotopes were
21 measured within the mineral apatite, with $\delta^{37}\text{Cl}$ values ranging from $+14.6 \pm 1.6 \text{ ‰}$ to $+40.0 \pm$
22 2.9 ‰ . These values expand the range previously reported for apatite in lunar rocks, and include
23 some of the heaviest Cl isotope compositions measured in lunar samples to date. The data here
24 do not display a trend between increasing rare earth elements contents and $\delta^{37}\text{Cl}$ values,
25 reported in previous studies. Other processes that can explain the wide inter- and intra-sample
26 variability of $\delta^{37}\text{Cl}$ values are explored. Magmatic degassing is suggested to have potentially
27 played a role in fractionating Cl isotope in these samples. Degassing alone, however, could not
28 create the wide variability in isotopic signatures. Our favored hypothesis, to explain small scale
29 heterogeneity, is late-stage interaction with a volatile-rich gas phase, originating from
30 devolatilization of lunar surface regolith rocks ~4 billion years ago. This period coincides with
31 vapor-induced metasomatism recorded in other lunar samples collected at the Apollo 16 and
32 17 landing sites, pointing to the possibility of widespread volatile-induced metasomatism on
33 the lunar nearside at that time, potentially attributed to the Imbrium formation event.

35 1. Introduction

36 Compared to most other planetary materials in the Solar System, lunar rocks are unique in
37 their wide-ranging chlorine isotopic signatures (Barnes et al., 2016; Boyce et al., 2015; Sharp
38 et al., 2010a; Tartèse et al., 2014a; Treiman et al., 2014). Lunar rocks display $\delta^{37}\text{Cl}$ signatures
39 [$^{37}\text{Cl}/^{35}\text{Cl}$ relative to standard mean ocean chloride (SMOC; 0.31977); Kaufmann et al., (1984)]
40 that range from ~ -4 ‰ up to $\sim +40$ ‰, which is in stark contrast to the Earth, where the reported
41 values cluster around $0 \text{ ‰} \pm 1 \text{ ‰}$ (Barnes et al., 2008; Sharp et al., 2007; Sharp et al., 2013).
42 This deviation in Cl isotope signatures, between the Earth and Moon, is contrary to the isotopic
43 similarity observed for most other elements, including oxygen (Herwartz et al., 2014; Wiechert
44 et al., 2001; Young et al., 2016), calcium (Dauphas et al., 2015; Valdes et al., 2014), chromium
45 (Lugmair and Shukolyukov, 1998), stable chromium (Bonnand et al., 2016), stable strontium
46 (Charlier et al., 2012), silicon (Armytage et al., 2011; Armytage et al., 2012; Zambardi et al.,
47 2013), titanium (Zhang et al., 2012), and zirconium (Schönbächler et al., 2003). Isotopic
48 similarities between the Earth and the Moon have been interpreted that the Moon, most likely,
49 formed from reconsolidation of proto-Earth material after a Moon forming event (Canup, 2012;
50 Canup et al., 2015; Čuk and Stewart, 2012; Rubie et al., 2015). Thus, Cl isotope fractionation
51 must have occurred during and/or after Moon formation and, therefore, provides unique insight
52 into volatile processing in/on the Moon.

53

54 Two competing mechanisms are believed to fractionate Cl isotopes in terrestrial systems:
55 (i) the lighter isotope ^{35}Cl is preferentially vaporized (Graham's Law), in volcanic gases for
56 example, while (ii) the heavier ^{37}Cl becomes incorporated into $\text{HCl}(\text{g})$ as a result of its
57 relatively high bond strength (Schauble et al., 2003) in systems where $\text{H} \gg \text{Cl}$ (Sharp et al.,
58 2010a). Most bulk primitive terrestrial basalts measured to date have $\delta^{37}\text{Cl}$ values clustering

59 around $\sim 0 \pm 2$ ‰, suggesting that these two fractionation mechanisms cancel each other out in
60 terrestrial systems (Sharp et al., 2013). To explain the elevated $\delta^{37}\text{Cl}$ values (i.e. > 0 ‰) of
61 lunar samples, Sharp et al. (2010a) favored the hypothesis in which lunar basaltic melts were
62 characterized by $\text{H} \ll \text{Cl}$, which promoted the degassing of Cl as metal chlorides (e.g., NaCl,
63 etc.) instead of $\text{HCl}(\text{g})$. This process would have preferentially incorporated the lighter isotope
64 ^{35}Cl into the degassed metal chloride phase, resulting in residual melts that were enriched in
65 ^{37}Cl (Sharp et al., 2010a).

66

67 Subsequent studies, of chlorine isotopes in lunar apatite, argued that preferential outgassing
68 of ^{35}Cl from erupting lavas was unlikely to be the main driver for the large Cl isotope
69 fractionation in lunar melts, notably because (i) apatite in plutonic samples tend to have higher
70 $\delta^{37}\text{Cl}$ values than apatite in erupted volcanic samples, and (ii) there seems to be a broad positive
71 correlations between chlorine isotopes and abundances (Boyce et al., 2015; Barnes et al., 2016).
72 Indicating that whatever mechanism(s) caused the extreme fractionation of chlorine isotopes
73 must have been capable of producing a reservoir that is rich in Cl, and is characterized by an
74 elevated Cl isotopic composition (Boyce et al., 2015). This assumption, and dismissal of
75 degassing as the mechanism for Cl isotope fractionation, is only valid if all samples had the
76 same initial Cl concentration and $\delta^{37}\text{Cl}$ value; a highly unlikely scenario.

77

78 In addition, positive correlations between apatite $\delta^{37}\text{Cl}$ values and some bulk-rock trace
79 element characteristics, such as La/Lu ratios and Th contents (Barnes et al., 2016; Boyce et al.,
80 2015), have been used to suggest heavy $\delta^{37}\text{Cl}$ are somehow linked to the involvement of a
81 KREEP (potassium (K), rare earth elements (REE), phosphorous (P)); (Warren and Wasson,
82 1979) component. Boyce et al. (2015) attributed large-scale Cl isotope fractionation to the

83 degassing of metal chlorides from the molten lunar magma ocean (LMO). In their model, the
84 elevated $\delta^{37}\text{Cl}$ values recorded by apatite, within the mare basalts, would have been acquired
85 during assimilation of a KREEP-component either (i) into the mare basalt source regions or (ii)
86 as the basalts ascended towards the lunar surface. While Barnes et al. (2016) suggested that the
87 ~34 to ~43 km of lunar crustal material (Wieczorek et al., 2013) was sufficiently thick to
88 prevent loss of Cl-bearing species from the LMO via continuous degassing, especially given
89 the high solubility of Cl in basaltic melts (Webster et al., 2009). Instead, they proposed that
90 crust-breaching impact events exposed KREEP-rich melt to low pressure environments,
91 promoting degassing of metal chlorides, and subsequent Cl isotope fractionation (Barnes et al.,
92 2016).

93

94 One of the heaviest lunar $\delta^{37}\text{Cl}$ values measured to-date, ~ +32 ‰, is from the granulite
95 sample 79215, whose signature is not thought to be from any process described above (Treiman
96 et al., 2014). This sample is characterized by an elevated P content (~200 × CI chondrite P
97 contents) but low K or REE contents (~10 × CI; e.g., P/Sm = ~20 Treiman et al. (2014)
98 suggested that in 79215, P, and the halogens, were largely added during vapor-phase
99 metasomatism, likely originating from impact-induced devolatilization of a KREEP-rich
100 target. Vapor-phase metasomatism is favored given that lunar conditions are too reduced for
101 abundant H_2O or CO_3^{2-} to be present and the lack of supporting evidence for fluid
102 metasomatism in lunar samples. This suggests that surface processes can also be responsible for
103 modifying Cl isotope composition in lunar samples.

104

105 Detailed understanding of the individual petrological histories of the rocks investigated in
106 Cl isotope studies is, therefore, critical to deciphering the mechanism(s) by which Cl isotopes
107 may have fractionated in lunar samples. In order to investigate the potential processes that

108 contributed to the elevated $\delta^{37}\text{Cl}$ values observed in lunar apatite, five Apollo 14 samples were
109 studied: high-Al basalts 14053 and 14072, a basaltic clast from breccia 14321,1482 and impact
110 melt rocks 14073 and 14310. These Apollo 14 samples have distinct petrogenetic histories, and
111 all pre-date the main period of mare volcanism, providing unique insight into the timing of,
112 and process(es) responsible for, Cl isotope fractionation in/on the Moon. Furthermore, the high
113 modal abundance and large size (typically $> 50 \mu\text{m}$ in the longest dimension) of apatite grains
114 in these samples permitted a thorough investigation of intra-grain and inter-sample variations
115 in volatile abundances and Cl isotope systematics.

116

117 **2. Apollo 14 High-Al rocks**

118 The Apollo 14 mission landed on the Fra Mauro Formation, which is part of the ejecta
119 blanket that formed from the excavation of the Imbrium Basin (Nemchin et al., 2009; Snape et
120 al., 2016). Mare Imbrium is the largest basin-affiliated mare deposit on the Moon (assuming
121 that the Procellarum KREEP Terrane is not an impact feature), and is thought to have excavated
122 lower lunar crust material during the basin-forming event (Nemchin et al., 2009). It remains
123 unclear, however, which Apollo 14 samples represent true Imbrium ejecta and which are
124 locally derived (Hiesinger and Head, 2006). The consistent dates obtained by $^{40}\text{Ar}/^{39}\text{Ar}$ dating
125 on whole rocks and fines (Alexander and Davis, 1974; Turner et al., 1972; Turner et al., 1971)
126 and Rb-Sr dating (Papanastassiou and Wasserburg, 1971; Compston et al., 1972; Compston et
127 al., 1972) of ~ 3.87 Ga were interpreted as representing the timing of formation of the Imbrium
128 Basin (Stöffler and Ryder, 2001; Wilhelms et al., 1987). Recent high-precision U-Pb dating of
129 phosphates and zircons in Apollo 14 impact melt breccias has provided an improved estimate
130 for the formation of the Imbrium Basin at ~ 3.93 Ga (Snape et al., 2016, and references therein).
131 Other studies of zircon grains from Apollo 14 lunar breccias have yielded U-Pb dates ranging
132 from ~ 4.0 to ~ 4.4 Ga, with distinct date peaks at ~ 4.35 and ~ 4.20 Ga (Meyer et al., 1996;

133 Nemchin et al., 2008), suggesting that a significantly older pre-Imbrium history is recorded by
134 the breccias. The temperature and shock effects associated with the development of the Fra
135 Mauro Formation were, therefore, sufficient to reset $^{40}\text{Ar}/^{39}\text{Ar}$ and Rb-Sr dates but not to reset
136 the zircon U-Pb systems in all samples (Nemchin et al., 2010).

137

138 Some basalts from the Fra Mauro region record volcanism older than 4 billion years on the
139 Moon (Neal and Kramer, 2006). Basaltic clasts from this region indicate a period of ~400
140 million years of volcanism, from ~4.3 to ~3.9 Ga (Compston et al., 1972; McKay et al., 1979;
141 Papanastassiou and Wasserburg, 1971; Snape et al., 2016), pre-dating the main period of mare
142 volcanism (Snyder et al., 2000). Volcanics from the Fra Mauro region may provide insights
143 into the evolution of the Moon from solidification of the crust, at around ~4.5 Ga to ~4.3 Ga
144 (Elkins-Tanton et al., 2011), to the beginning of the main period of mare volcanism that
145 commenced around ~3.85 Ga (Shearer et al., 2006). Crystallization and/or impact-resetting
146 ages for all the Apollo 14 samples studied here are given in Table 1, and range between ~4.1
147 Ga and ~3.8 Ga (Compston, et al., 1972; Dasch et al., 1987; Hui et al., 2013; Husain et al.,
148 1971; Mark et al., 1974; Papanastassiou and Wasserburg, 1971; Tatsumoto et al., 1972; Turner
149 et al., 1972; York et al., 1972).

150

151 In addition to their old age, the Apollo 14 basalts are also geochemically distinct in that
152 they are relatively enriched in Al_2O_3 (11 – 16 wt.%), leading to their classification as ‘high-Al’
153 basalts (Neal and Kramer, 2006; Ridley, 1975). Two petrological models have been proposed
154 for the formation of these high-Al samples: (1) “pristine” volcanic rocks that formed solely
155 through endogenous lunar processes and (2) impact generated melts referred to as “impact
156 melts” (Hui et al., 2011).

157

158 Based on incompatible trace element (ITE) abundances and crystallization ages, the Apollo
159 14 high-Al basalts have been separated into three distinct groups: Group A (~4.3 Ga), Group
160 B (~4.1 Ga), and Group C (~3.9 Ga) (Neal and Kramer, 2006). Samples within these groups
161 are thought to be related via a closed-system crystal fractionation model for Group A, and an
162 open-system evolution model, involving assimilation of a KREEP component and/or granitic
163 melts, for Groups B, and C (Hui et al., 2011; Neal et al., 1988; Neal et al., 1989; Neal and
164 Kramer, 2006; Neal and Taylor, 1989). The main geochemical features of the samples studied
165 here are summarized in Table 1. The impact-melt samples, 14073 and 14310, are crystallization
166 products of impact-melted lunar regolith and/or feldspathic crust (Schonfeld and Meyer,
167 Charles, 1972), and could have inherited their high-Al contents from melting of anorthosite-
168 rich targets (Hui et al., 2011). In contrast, for the endogenous pristine basalts (14053, 14072,
169 and 14321,1482), the high-Al content is not related to any contribution from the melting of
170 anorthosite-rich rocks and it is more likely that elevated Al contents were directly inherited
171 from the mantle source regions of these basalts (Hui et al., 2011; Neal and Kramer, 2006).
172 These different formational mechanisms have been used to explain the compositional
173 differences between the Apollo 14 pristine basalts and impact melt samples. Detailed
174 descriptions of all the samples studied here is given in the Supplementary Material.

175

176 **3. Analytical techniques**

177 Before secondary ion mass spectrometry (SIMS) measurements, each polished thin-section
178 was carbon-coated and studied using a dual beam FEI Quanta 3D Scanning Electron
179 Microscope (SEM) at The Open University, following the protocol described in Tartèse et al.
180 (2013). The SEM was used to locate apatite crystals suitable for SIMS analyses, and to
181 characterize the petrographic context of each grain. The carbon coat was removed after SEM
182 work and the samples were cleaned with isopropanol and stored in a vacuum oven at ~55 °C

183 for a minimum of 48 hours. Subsequently, samples were coated with ~30 nm of gold using an
184 EMITECH K575X peltier cooled gold sputter coater. After coating, the samples were
185 immediately loaded into the Cameca NanoSIMS 50L at The Open University. Apatite was
186 located following initial pre-sputtering for several minutes of large ($>10 \times 10 \mu\text{m}$) areas.
187 Smaller $\sim 8 \times 8 \mu\text{m}$ areas, containing the target apatite grains, were then pre-sputtered by
188 rastering a Cs^+ beam of $\sim 40 \text{ pA}$ with an accelerating voltage of 16 kV for ~ 2 minutes, in order
189 to clean the target surface. For analysis, the 40 pA probe was then rastered over $\sim 4 \times 4 \mu\text{m}$
190 areas in the apatite grains for ~ 4 minutes. An electron flood gun was used for charge
191 compensation. During analysis the vacuum in the analysis chamber remained around $\sim 5 \times 10^{-9}$
192 Torr. The NanoSIMS was tuned to achieve a mass resolving power of ~ 8000 and the negative
193 secondary ions of $^{16}\text{O}^1\text{H}$, ^{18}O , ^{19}F , ^{35}Cl , ^{37}Cl , and $^{40}\text{Ca}^{19}\text{F}$ were collected simultaneously on
194 electron multipliers. ^{19}F ions were monitored, but only for $\sim 66\text{s}$ per analysis to avoid saturating
195 the detectors.

196

197 The abundances of Cl, F, and H_2O were calibrated using the published Cl, F, and H_2O
198 contents and the measured $^{35}\text{Cl}/^{18}\text{O}$, $^{19}\text{F}/^{18}\text{O}$, and $^{16}\text{OH}/^{18}\text{O}$ ratios of Ap004 and Ap018
199 reference apatite crystals mounted in epoxy resin (McCubbin et al., 2012). Background
200 measurements of Cl and OH were collected on San Carlos olivine and nominally anhydrous
201 minerals within sample sections ($\sim 100 \text{ ppm H}_2\text{O}$ and $\sim 4 \text{ ppm Cl}$) and were subtracted from the
202 measured values. Reported uncertainties for abundances incorporate the 2σ uncertainty of the
203 calibration slopes and analytical uncertainties associated with individual measurements. Ap004
204 was used to correct the measured $^{37}\text{Cl}/^{35}\text{Cl}$ ratios of unknown samples for instrumental mass
205 fractionation ($\text{IMF}; (^{37}\text{Cl}/^{35}\text{Cl}_{\text{unknown}}/^{37}\text{Cl}/^{35}\text{Cl}_{\text{standard}})-1) \times 1000$). The Cl isotope composition is
206 reported using standard delta notation with respect to $^{37}\text{Cl}/^{35}\text{Cl}$ of standard mean ocean
207 chloride. Isotope measurements are reported with their associated 2σ uncertainties, which

208 combine the reproducibility of the $^{37}\text{Cl}/^{35}\text{Cl}$ measurements on an appropriate standard and the
209 internal uncertainty of each analysis.

210

211 **4. Results**

212 In the following section, textural descriptions and $\delta^{37}\text{Cl}$ values of apatite, with
213 corresponding Cl and H₂O abundances, are given for each sample. High-resolution back-
214 scattered electron (BSE) images including the petrographic setting of individual apatite grains
215 analyzed in this study are shown in Supplementary Figures SM2 to 6. The results of NanoSIMS
216 analyses of apatite for Cl isotopic compositions and H₂O and Cl abundances are listed in Table
217 2. In addition F abundances for apatite in some samples are listed in Table 2.

218

219 *4.1. 14053,19*

220 In sample 14053,19 eight analyses were carried out in seven apatite crystals occurring in
221 four separate areas (Fig. SM2A-D). Apatite crystals in this sample are all associated with
222 mesostasis. Here, mesostasis regions were identified by the breakdown of fayalite into Fe metal
223 (often described as ‘spongy’ Fe in the literature (Taylor et al., 2004)) and silica-rich glass, as
224 well as the presence of a diverse range of phases with relatively small grain sizes (<20 μm in
225 the longest dimension; Potts et al., 2016). All of the apatite grains measured here were
226 subhedral to anhedral, >10 μm in the longest dimension, and were found associated with
227 quenched K-rich glass. The majority of apatite grains in this section were also found in contact
228 with plagioclase, except Ap#4a and Ap#4b.

229

230 The volatile abundances of apatite in 14053 overlap with those of Mg- and alkali- suite
231 rocks (Fig. 1), which are fluorapatite with greater amounts of Cl than H₂O. The $\delta^{37}\text{Cl}$ values of
232 apatite in 14053,19 range from $+15.6 \pm 2.2 \text{ ‰}$ to $+34.3 \pm 2.9 \text{ ‰}$. H₂O abundances of apatite in
233 this sample range from $89 \pm 4 \text{ ppm}$ to $1662 \pm 80 \text{ ppm}$ (Fig. 2A; Table 2). The Cl concentrations
234 of apatite in this sample range from $1569 \pm 2 \text{ ppm}$ to $16054 \pm 17 \text{ ppm}$ (Fig. 2B; Table 2).
235 Apatite 4a shows the highest $\delta^{37}\text{Cl}$ value ($+34.3 \pm 2.9 \text{ ‰}$) whilst having the lowest H₂O content
236 ($89 \pm 4 \text{ ppm}$) and highest Cl content ($16054 \pm 17 \text{ ppm}$) of any apatite measured from this
237 sample. In contrast, Ap#1 has the lowest $\delta^{37}\text{Cl}$ value ($+15.6 \pm 2.2 \text{ ‰}$) measured from this
238 sample and the highest H₂O content ($1662 \pm 80 \text{ ppm}$) and lowest Cl content ($1569 \pm 2 \text{ ppm}$).
239 Both apatite crystals Ap#4a and Ap#1 are found within mesostasis regions although there
240 appears to be significantly more fayalite reduction surrounding Ap#4a than Ap#1. Overall,
241 there are strong correlations between increasing $\delta^{37}\text{Cl}$ values and (a) decreasing H₂O
242 abundances and (b) increasing Cl abundances for apatite in 14053,19 (Fig. 2A-B). There is
243 little intra-region variation, in terms of $\delta^{37}\text{Cl}$, in this section except for Area #1 in which the
244 two analyses yielded a difference of $\sim 12 \text{ ‰}$. The two heaviest values ($> +32 \text{ ‰}$) in this section
245 are from two apatite grains within the same region (area 4), which displays the highest
246 proportion of reduction-related texture. Apatite grains in this region also display resorbed edges
247 compared to apatite within areas 1 and 5 that are characterized by $\delta^{37}\text{Cl}$ values around $+23$ to
248 $+28 \text{ ‰}$ (except Ap#1). Apatite grains within area 8 also appear to have resorbed edges, and
249 have $\delta^{37}\text{Cl}$ values of between $+21$ and $+24 \text{ ‰}$. The subhedral apatite grains within areas 1 and
250 5 have higher H₂O contents ($>500 \text{ ppm}$) compared to the anhedral apatite grains within area 4
251 ($<200 \text{ ppm}$). The highest Cl contents have been measured in the subhedral grains found in area
252 4.

253

254 *4.2. 14072,13*

255 In sample 14072,13 five analyses were carried out in five distinct apatite crystals occurring
256 in four different areas (Fig. SM3A-E where B and C are both part of one larger area). All apatite
257 crystals were found within mesostasis regions that were texturally similar to those in 14053,19,
258 although mesostasis regions in 14072,13 generally contained a larger fraction (>30 modal %) of
259 spongy Fe. Large (> 20 μm) euhedral to sub-euhedral apatite yielded $\delta^{37}\text{Cl}$ values ranging
260 from $+16.3 \pm 2.9 \text{ ‰}$ to $+40.0 \pm 2.9 \text{ ‰}$, with Cl and H_2O abundances ranging from 4167 ± 5 to
261 14759 ± 15 ppm and 117 ± 6 to 189 ± 9 ppm, respectively (Figs. 2A-B; Table 2).

262

263 The volatile abundances of apatite in this thin-section overlap with those of Mg- and alkali-
264 suite rocks (Fig. 1). Unlike sample 14053,19, there is no clear correlation between apatite Cl
265 or H_2O abundance and the associated $\delta^{37}\text{Cl}$ values in 14072,13 (Fig. 2). All of the apatite grains,
266 except in area 7, are in contact with spongy Fe- and K-rich glass, while the mesostasis pockets
267 are surrounded by plagioclase. The lower $\delta^{37}\text{Cl}$ values of around +16 to +20 ‰ have been
268 measured in euhedral apatite grains, while the heaviest $\delta^{37}\text{Cl}$ values ($+28.8 \pm 2.9 \text{ ‰}$ and $+40.0$
269 $\pm 2.9 \text{ ‰}$) are associated with anhedral crystals. This relationship is broadly consistent with
270 what we observed in sample 14053,19.

271

272 *4.3. 14321,1482*

273 In sample 14321,1482 four analyses were carried out in three apatite crystals occurring in
274 three different areas (Fig. SM4A-C). Apatite crystals in 14321,1482 are euhedral to subhedral,
275 > ~10 μm in the longest dimension, and were located in mesostasis regions, which contain
276 spongy Fe in areas 3 and 5, fayalite, silica, and K-rich glass.

277

278 The apatite $\delta^{37}\text{Cl}$ values range from $+20.1 \pm 0.9 \text{ ‰}$ to $+28.6 \pm 1.1 \text{ ‰}$ and are associated
279 with Cl abundances of $\sim 5000\text{-}8000$ ppm and very low H_2O contents < 150 ppm (Figs. 2A-B;
280 Table 2). Although limited in number, the analyses of 14321,1482 are consistent with the
281 ranges of Cl abundances and $\delta^{37}\text{Cl}$ values measured in most of the apatite grains from samples
282 14053 and 14072. The lowest $\delta^{37}\text{Cl}$ value in this sample has been measured in area 5 on an
283 anhedral apatite grain in this section, opposite to observations for 14053 and 14072. This grain
284 also is in direct contact with spongy Fe. The other apatite grains within this sample have $\delta^{37}\text{Cl}$
285 values between $\sim +24$ and $+29 \text{ ‰}$ and are all euhedral to subhedral.

286

287 *4.4. 14073,9*

288 In sample 14073,9 fifteen analyses were carried out on nine apatite crystals occurring in
289 five different areas (Fig. SM5A-E). All apatite grains in this sample were located in mesostasis
290 regions, identified by the presence of K-rich glass. The mesostasis regions in 14073, however,
291 are texturally and compositionally different from those in 14053 and 14072, as they do not
292 contain spongy Fe, but interstitial K-rich glass associated with K-feldspar. The apatite grains
293 analyzed here are subhedral, up to $50 \mu\text{m}$ in the longest dimension, and are all in contact with
294 K-rich glass, with some containing melt inclusions.

295

296 The analyzed apatite grains are H_2O -poor and Cl-rich compared to typical mare basalts
297 (Fig. 1). The $\delta^{37}\text{Cl}$ values of apatite from sample 14073,9 display a large range from $+16.5 \pm$
298 2.2 ‰ to $+36.9 \pm 2.1 \text{ ‰}$, most of the them clustering between $\sim +21$ and $+28 \text{ ‰}$ (Fig. 2A-B).
299 The Cl and H_2O abundances of these apatite range from 580 ± 1 ppm to 16149 ± 18 ppm and

300 291 ± 14 ppm to 1081 ± 52 ppm, respectively. Generally, the higher $\delta^{37}\text{Cl}$ values correspond
301 to low to moderate H_2O contents, while there is no strong correlation between $\delta^{37}\text{Cl}$ values and
302 Cl abundances (Fig. 2). In some mesostasis areas, such as area 11 (a cluster of apatite crystals)
303 in which 5 analyses were carried out, apatite crystals are fairly homogeneous in terms of
304 abundances of H_2O (317 ± 15 ppm to 419 ± 20 ppm) and Cl (1241 ± 2 ppm to 1648 ± 2 ppm)
305 and Cl isotopic composition ($+21.0 \pm 2.2$ ‰ to 27.5 ± 2.6 ‰). In other areas, the intra-region
306 variations of $\delta^{37}\text{Cl}$ are large, ranging from $+16.5 \pm 2.2$ ‰ to $+27.7 \pm 2.0$ ‰ within a single
307 apatite grain (Ap#12), and between $+25.7 \pm 1.9$ ‰ and $+36.9 \pm 2.1$ ‰ in a single grain analyzed
308 in area 19.

309

310 *4.5. 14310,171*

311 Seven analyses were made across four apatite crystals in three areas (Figs. SM6A-C) in
312 thin section 14310,171. Generally apatite was found in mesostasis regions in this sample,
313 although these areas noticeably lack the large amount of K-rich glass observed in other Apollo
314 14 mesostasis regions, particularly 14073,9. The apatite grains in 14310,171 are euhedral to
315 subhedral, with the size varying from $> \sim 30$ μm to ~ 10 μm in the longest dimension. Apatite is
316 associated with pyroxene, plagioclase, K-feldspar, merrillite, and ilmenite. The $\delta^{37}\text{Cl}$ values
317 for apatite in this sample range from $+14.6 \pm 1.6$ ‰ to $+25.3 \pm 2.0$ ‰, and apatite Cl and H_2O
318 abundances range from 4597 ± 8 ppm to 11256 ± 19 ppm and 95 ± 3 to 354 ± 11 ppm,
319 respectively (Table 2). Similarly to apatite in sample 14073,9, elevated $\delta^{37}\text{Cl}$ values tend to be
320 associated with lower H_2O abundances (Fig. 2A). In this sample, the higher $\delta^{37}\text{Cl}$ values also
321 tend to be associated with higher Cl abundances (Fig. 2B). As in sample 14073,9, the degree
322 of intra-region heterogeneity in $\delta^{37}\text{Cl}$ values varies across the sample, particularly in area 4.
323 The euhedral apatite grains in this section have the lower $\delta^{37}\text{Cl}$ values ($< +18$ ‰), while the

324 heavier Cl isotope values are associated with a smaller (<10 μm) subhedral apatite grain, apart
325 from those in area 1.

326

327 5. Discussion

328 This study provides a comprehensive dataset on the chlorine isotopic compositions of
329 apatite from Apollo 14 samples, including both igneous high-Al basalts and impact melt rocks.
330 As shown in Figure 3, the $\delta^{37}\text{Cl}$ values measured here mostly cluster within a range of between
331 +15 and +35 ‰, which is consistent with the upper end of the range of $\delta^{37}\text{Cl}$ values measured
332 in high- and low-Ti mare basalts and with those obtained on KREEP-rich samples (Barnes et
333 al., 2016; Boyce et al., 2015; Sharp et al., 2010a; Tartèse et al., 2014a; Treiman et al., 2014).
334 The heaviest $\delta^{37}\text{Cl}$ values, of around +35 to +40 ‰, were measured in apatite from samples
335 14053, 14072, and 14073 and are comparable to the heaviest $\delta^{37}\text{Cl}$ values reported for KREEP-
336 rich basalts (Sharp et al., 2010a; Barnes et al., 2016) and KREEP-rich intrusive rocks of the
337 Mg-suite (Treiman et al., 2015; Barnes et al., 2016). The unique petrogeneses of the Apollo 14
338 samples studied here provide an opportunity to evaluate the potential mechanisms for Cl
339 isotope fractionation under lunar magmatic conditions.

340

341 5.1. Linking assimilation of KREEP to the Cl isotope composition of magmatic apatite

342 Magmatic degassing of chlorine from the LMO, in the form of metal chlorides, has been
343 invoked to explain the elevated chlorine isotopic compositions of lunar samples (Boyce et al.,
344 2015; Barnes et al., 2016). This hypothesis results in an enrichment of ^{37}Cl in the KREEP-rich
345 residual melts of the LMO, and is supported by the positive correlations observed between
346 bulk-rock incompatible trace element contents (REE, Th) and apatite $\delta^{37}\text{Cl}$ values (Fig. 4). Our
347 analyses of apatite in five Apollo 14 samples, however, do not show any correlation between

348 KREEP component (e.g. elevated La/Lu ratios in bulk samples) and elevated $\delta^{37}\text{Cl}$ values (Fig.
349 4). Petrologically, the high-Al pristine basalts 14053, 14072, and 14321,1482 are all believed
350 to have assimilated an evolved KREEP-rich component even though they are not *sensu stricto*
351 KREEP-basalts (Hui et al., 2011; Neal et al., 1988; Neal and Kramer, 2006). The impact melt
352 samples 14073 and 14310 also contain a significant KREEP component (El Goresy et al., 1971;
353 McKay et al., 1979) but are thought to have formed via the melting of feldspathic regolith or
354 anorthosite material (Hui et al., 2011; Schonfeld et al., 1972). The Apollo 14 samples studied
355 here thus suggest that additional magmatic and/or post-crystallization processes can modify
356 apatite $\delta^{37}\text{Cl}$ values.

357

358 *5.2. Volatile abundances in Apollo 14 apatite*

359 All of the apatite analyzed here are F-rich, with compositions clustering around the F apex
360 of the apatite volatile ternary (Fig. 1). Volatile compositions of apatite in samples 14072,
361 14310, and 14321,1482 plot almost exclusively along the F-Cl binary, in the field typically
362 occupied by apatite from lunar highland samples. Apatite compositions for 14053 and 14073
363 have a greater H₂O component, consistent with the apatite compositions of KREEP-rich basalts
364 and relatively H₂O-poor mare basalts (Barnes et al., 2014, 2013; Boyce et al., 2010; Greenwood
365 et al., 2011; McCubbin et al., 2015b, 2011, 2010a, 2010b; Tartèse et al., 2014; Tartèse et al.,
366 2013; Tartèse et al., 2014b).

367

368 The range of measured water contents within apatite in high-Al basalt 14053 (~90 - 1660
369 ppm H₂O) is similar to the range obtained in previous studies of this sample, from around 200
370 ppm up to ~2400 ppm H₂O (Greenwood et al., 2011; Boyce et al., 2010; McCubbin et al., 2010;
371 Pernet-Fisher et al., 2014). Similarly, previously measured apatite Cl contents of ~0.17 to 0.47

372 wt.% in 14053 (Boyce et al., 2010; McCubbin et al., 2010) are within the range of apatite Cl
373 abundances measured here (~0.16 to 1.6 wt.%).

374

375 Determining the volatile content of the melt from which apatite crystallized, based on the
376 measured volatile contents of apatite, is not trivial given that F, Cl, and OH (reported here as
377 H₂O) share the crystallographic X-site within the apatite crystal lattice. As such, volatiles are
378 essential structural components, meaning that simple Nernst partitioning behavior cannot be
379 applied (Boyce et al., 2014; McCubbin et al., 2015). Apatite, however, is generally considered
380 a major sink for F in crystallizing melts (McCubbin, et al, 2015) as crystal chemistry favors
381 preferential incorporation of F, over OH and Cl, into apatite (Boyce et al., 2014; Kusebauch et
382 al., 2015). As F is incorporated into apatite and/or lost via degassing (Ustunisik et al., 2015;
383 Ustunisik et al., 2011), total F in the melt would decrease with crystallization, meaning primary
384 apatite would have higher F contents than later grown apatite. If all the samples began with
385 similar F melt content and Cl isotope ratios, this could suggest that apatite with greater F
386 abundances record the initial $\delta^{37}\text{Cl}$ values of their respective melts. Apatite grains with lower
387 F abundance would, therefore, have grown later and record the $\delta^{37}\text{Cl}$ isotopic compositions of
388 the melt at the more advanced stages of crystallization. There is a vague correlation between
389 increasing $\delta^{37}\text{Cl}$ values and decreasing F abundance of apatite (Fig. 5). In sample 14321,1482
390 there are very few F measurements, so we cannot ascertain whether we have analyzed early
391 growing apatite, there is only one stage of apatite growth, or there is no change in apatite F
392 contents (and Cl isotope signatures) with melt evolution. For 14310, there is some correlation
393 between F abundances and $\delta^{37}\text{Cl}$ values (Fig. 5). Overall, the rough trend displayed by most
394 apatite analysis in samples 14053, 14072, and 14073 could suggest that the initial $\delta^{37}\text{Cl}$ values
395 of the Apollo 14 melts were around $\sim 20 \pm 5 \text{ ‰}$ and that subsequent melt evolution has imparted
396 heavier $\delta^{37}\text{Cl}$ signatures. It is important to stress that this interpretation is only valid if F

397 contents and Cl isotope ratios were similar throughout different melts. The different
398 petrogeneses of these samples also suggests it is unlikely they began with the same volatile
399 abundance and isotope signatures. Importantly, however, if crystal chemistry controls
400 dominate apatite compositions, then the chlorine isotopic compositions of apatite can only be
401 explained by increasing the $^{37}\text{Cl}/^{35}\text{Cl}$ of the melt, or apatite after crystallization.

402

403 *5.3. Solar-wind implantation*

404 Apollo 14 sample 14053 is thought to have crystallized as a typical high-Al basalt, but the
405 outer sections were later affected by solar-wind H implantation during its residence in the lunar
406 regolith (Taylor et al., 2004). Subsequently, subsolidus thermal metamorphism (likely induced
407 from ejecta blanket heat) facilitated the permeation of solar-wind H into the rock and led to
408 reduction of localized areas, characterized by reduction-breakdown textures of fayalite to Fe-
409 metal and silica, identified by the below reaction (Taylor et al., 2004).

410



412

413 These reduction-breakdown textures, identified by the presence of Fe-metal and silica, are
414 shown in Figures SM2A, 2B, and 2D. Reduction-breakdown textures are also seen in 14072,
415 and to a smaller extent in 14321,1482. It has also been suggested that La_2O_3 and Ce_2O_3 contents
416 in apatite from 14053, in contact with reduced areas, may have undergone secondary alteration
417 as a consequence of H-reduction (Taylor et al., 2004). If such metamorphism occurred then it
418 is conceivable that the volatile abundances and isotopic composition of apatite in these samples
419 may have been modified (Boyce et al., 2010; Greenwood et al., 2011).

420

421 The lack of reduction textures in 14310 and 14073 is important given that these rocks
422 formed from impact melt processing of the lunar regolith, indicating that either (i) such a
423 signature was erased during impact melting or (ii) that these samples did not undergo the
424 surface reduction process, unlike the other samples studied. The second scenario would support
425 late alteration of 14053 (and potentially 14072, as well as 14321,1482) and negligible solar-
426 wind alteration of 14310 and 14073.

427

428 *5.4. The role of volatile degassing from lunar magmas*

429 Chlorine is incompatible in the major silicate minerals that crystallize from basaltic melts
430 (e.g. Webster et al., 2009). When Cl reaches saturation it will partition into the vapor phase,
431 and degas from basaltic melts (Boyce and Hervig, 2008; Patiño Douce and Roden, 2006;
432 Shinohara, 2009; Ustunisik et al., 2011; Ustunisik et al., 2015; Webster et al., 1999). Sharp et
433 al. (2010b) suggested that under anhydrous lunar magmatic conditions the bonding potentials
434 of both isotopes (^{35}Cl and ^{37}Cl) are similar. The kinetic loss of ^{35}Cl is not cancelled out by the
435 loss of ^{37}Cl via bond incorporation (e.g. $\text{HCl}_{(g)}$). The melt is then enriched in ^{37}Cl explaining
436 the heavy $\delta^{37}\text{Cl}$ values acquired by late-crystallizing apatite. Theoretical modeling of Cl isotope
437 fractionation during degassing of metal chloride species indicates that a $\delta^{37}\text{Cl}$ increase of up to
438 20 ‰ is expected for 95% Cl loss as FeCl_2 (Sharp et al., 2010a; Ustunisik et al., 2015), which
439 could explain the range in $\delta^{37}\text{Cl}$ values exhibited by apatite from most mare basalt samples
440 (Barnes et al., 2016; Boyce et al., 2015; Sharp et al., 2010a; Tartèse et al., 2014a). It is important
441 to note that the $\text{H} \ll \text{Cl}$ conditions required in the Sharp et al. (2010a) model does not
442 necessarily imply that lunar melts were dry, but it does require melt $\text{H} \ll \text{Cl}$ at the time of Cl
443 degassing. It should also be noted that other lines of evidence for magmatic degassing from
444 lunar melts is recorded in the literature, through coatings on glass beads (McKay et al., 1972),

445 fractionations of H (Hauri et al., 2015 and references therein), and C (Wetzel et al., 2015)
446 isotope systems. The large inter- and intra-sample $\delta^{37}\text{Cl}$ variations measured in apatite across
447 Apollo samples, with vastly different petrogenesis seem difficult.

448

449 *5.5. Vapor-phase interactions*

450 Near-surface fractionation of Cl isotopes via Cl evaporation (as HCl, as well as organic and
451 metal compounds) has been suggested as a potential mechanism to induce fractionation in
452 terrestrial systems (Gola et al., 2005), which is supported by modelling (Richet et al., 1977), as
453 well as experimental work (Huang et al., 1999; Liebscher et al., 2006), and thought to be
454 responsible for elevated signatures ($\sim 32\text{‰}$) in lunar granulite 79215 (Treiman et al., 2014). It
455 is, therefore, conceivable that a volatile-rich vapor, enriched in ^{37}Cl , interacted with the late-
456 stage Apollo 14 basaltic and impact melts, similar to what has been proposed by Treiman et al.
457 (2014) to account for elevated apatite $\delta^{37}\text{Cl}$ values in granulite 79215. Vapor phase
458 crystallization of a variety of minerals, including oxides, halides, iron, and alkali, has been
459 reported in vugs within Apollo 14 breccias (McKay et al., 1972). This vapor phase, noted to
460 have contained chlorides, has been attributed to thermal metamorphism immediately following
461 the deposition of the Fra Mauro ejecta blanket from the Imbrium Basin (McKay et al., 1972),
462 the source of which would be a volatile-rich rock in the shallow crust. Thermal metamorphism
463 has also been attributed to Apollo 14 volcanic rocks 14053 and 14072 undergoing subsolidus
464 alteration, as mentioned above (Taylor et al., 2004).

465

466 Vapor-phase metasomatism could have enriched individual mesostasis regions in Cl with
467 minimal effect on their H_2O budgets (if the metasomatic agent was low in H for example), and,
468 at the same time, increased apatite $\delta^{37}\text{Cl}$ values. Such mechanism could, therefore, induce

469 heterogeneous increase of apatite $\delta^{37}\text{Cl}$ values and Cl contents depending on the timing and
470 degree of interaction. No strong correlation between apatite Cl and H_2O abundances and $\delta^{37}\text{Cl}$
471 values is expected in this scenario since measured abundances would be variable depending on
472 the initial apatite volatile contents. Such a process could also create variations of apatite volatile
473 abundances and isotopic compositions from grain to grain and from mesostasis area to
474 mesostasis area in a single sample depending on the apatite size or the local permeability, for
475 example. In the case of granulite 79215, Treiman et al. (2014) suggested that the addition of P
476 and halogens due to vapor-phase metasomatism triggered growth of large apatite crystals
477 characterized by homogeneous, elevated $\delta^{37}\text{Cl}$ values. Although in this same sample, 79215,
478 Barnes et al. (2016) found variations in $\delta^{37}\text{Cl}$ values on the order of $\sim 10\%$. Furthermore, the
479 Treiman et al. (2014) study suggested apatite crystallization in 79215 was induced from P-rich
480 vapor. Recent work, on S abundances in lunar apatite, has also suggested that metasomatic
481 alteration by a S-Cl-bearing volatile phase is responsible for Cl-S zoning observed in apatite in
482 some mare basalts (Konecke et al., 2017). During the final stages of solidification of the studied
483 Apollo 14 samples, a metasomatic agent could have interacted with the melt, altering Cl isotope
484 ratios and abundances. The large variation in $\delta^{37}\text{Cl}$ values could thus suggest that some apatite
485 formed prior to interaction with a metasomatic agent, while others grew after variable
486 metasomatism. It is also plausible that the high-Al basalts assimilated vapor phase products
487 during lava flow on the lunar surface, in a similar way to how variable amounts of KREEP
488 material were assimilated to these basalts (Hui et al., 2011; Hui et al., 2013). This variability
489 in assimilation, and in the original Cl isotope signatures of vapor phase products, could account
490 for the large inter- and intra-sample heterogeneity of Cl isotopes observed in these samples.

491

492 It has been suggested that lunar ejecta blankets, such as the Fra Mauro unit, could have
493 initiate non-volcanic fumarole activity (McKay et al., 1972). Vapors released during
494 crystallization within hot zones (~ 1000 °C) percolate up through colder zones where non-
495 condensable gases (i.e. Cl) may escape through the ejecta blanket forming fumaroles (Fig. 6;
496 Shearer et al., 2014). This process has also been identified in ‘rusty-rock’ 66095 (Shearer et
497 al., 2014) and is similar to the mechanism proposed to explain crystallization of large apatite
498 with elevated $\delta^{37}\text{Cl}$ values in granulite 79215 (Treiman et al., 2014). Vapor condensation has
499 also been proposed as a mechanism to explain volatile contents in lunar glass beads (74220,
500 15426) and 66095 (Day et al., 2017). The two samples, 66095 and 79215, have yielded dates
501 around 3.9 Ga (Fischer-Gödde and Becker, 2012; Norman et al., 2006; Snape et al., 2017),
502 similar to the Apollo 14 samples studied here (Table 1). Altogether, these samples hint at the
503 widespread occurrence of vapor-related metasomatism during a period when the impact flux
504 on the lunar surface may have been particularly high (Gomes et al., 2005; Morbidelli et al.,
505 2012; Tera et al., 1974). As samples 66095 and 79215 are from landing sites on the western
506 limb of the nearside, this work extends the geographical occurrence of vapor-rich
507 metasomatism on the lunar surface to include the Apollo 14 site on the mid-eastern section of
508 the nearside, hinting at large-scale volatile release during this period, possibly related to the
509 Imbrium impact event.

510

511 **6. Conclusions**

512 Understanding processes that have affected the volatile contents and isotopic compositions
513 of lunar samples is important for constraining the volatile budget of the lunar interior. The
514 Apollo 14 samples studied here have provided an opportunity to explore the various processes
515 that can fractionate Cl isotopes in lunar magmatic and surface environments. The interaction

516 with a KREEP component, during the Apollo 14 samples petrogenesis, is expected to have
517 imprinted an elevated $\delta^{37}\text{Cl}$ signature. Instead, other process(es) must be responsible for the
518 wide-range, elevated, $\delta^{37}\text{Cl}$ values of the Apollo 14 samples investigated. We propose that
519 magmatic degassing, as first suggest by Sharp et al. (2010) could explain the elevated $\delta^{37}\text{Cl}$
520 signature of Apollo 14 melts but that this process alone could not account for the variability of
521 isotopic signatures observed in these rocks. The mechanism we ultimately favor, to explain the
522 large intra- and inter-sample variability in $\delta^{37}\text{Cl}$ isotope values measured, is variable interaction
523 of late-stage melts with a Cl-rich vapor-phase. The presence of vapor-induced metasomatism
524 in these samples points to the presence of wide-spread fumarolic activity on the nearside of the
525 Moon at ~ 4 Ga.

526

527 **Acknowledgements**

528 We thank NASA CAPTEM for the allocation of Apollo samples. STFC is thanked for a
529 PhD studentship to N.J.P and a research grant to M.A. and I.A.F. (grant number ST/I001298/1).
530 NanoSIMS access was through UKCAN funded through STFC grant ST/1001964/1. Zachary
531 Sharp and two anonymous reviewers are thanked for their constructive comments.

532 **References**

- 533 Alexander E. C. and Davis P. K. (1974) ^{40}Ar - ^{39}Ar ages and trace element contents of Apollo 14
534 breccias; an interlaboratory cross-calibration of ^{40}Ar - ^{39}Ar standards. *Geochim. Cosmochim.*
535 *Acta* **38**, 911–928.
- 536 Armytage R. M. G., Georg R. B., Savage P. S., Williams H. M. and Halliday A. N. (2011) Silicon
537 isotopes in meteorites and planetary core formation. *Geochim. Cosmochim. Acta* **75**, 3662–3676.
- 538 Armytage R. M. G., Georg R. B., Williams H. M. and Halliday A. N. (2012) Silicon isotopes in lunar
539 rocks: Implications for the Moon's formation and the early history of the Earth. *Geochim.*
540 *Cosmochim. Acta* **77**, 504–514.
- 541 Barnes J. D., Sharp Z. D. and Fischer T. P. (2008) Chlorine isotope variations across the Izu-Bonin-
542 Mariana arc. *Geology* **36**, 883.
- 543 Barnes J. D., Sharp Z. D., Fischer T. P., Hilton D. R. and Carr M. J. (2009) Chlorine isotope

- 544 variations along the Central American volcanic front and back arc. *Geochemistry, Geophys.*
545 *Geosystems* **10**, 1–17.
- 546 Barnes J. J., Franchi I. a., Anand M., Tartèse R., Starkey N. a., Koike M., Sano Y. and Russell S. S.
547 (2013) Accurate and precise measurements of the D/H ratio and hydroxyl content in lunar
548 apatites using NanoSIMS. *Chem. Geol.* **337–338**, 48–55.
- 549 Barnes J. J., Tartèse R., Anand M., McCubbin F. M., Franchi I. A., Starkey N. A. and Russell S. S.
550 (2014) The origin of water in the primitive Moon as revealed by the lunar highlands samples.
551 *Earth Planet. Sci. Lett.* **390**, 244–252.
- 552 Barnes J. J., Tartèse R., Anand M., McCubbin F. M., Neal C. R. and Franchi I. A. (2016a) Early
553 degassing of lunar urKREEP by crust-breaching impact(s). *Earth Planet. Sci. Lett.* **447**, 84–94.
- 554 Barnes J. J., Tartèse R., Anand M., McCubbin F. M., Neal C. R. and Franchi I. A. (2016b) Early
555 volatile degassing on the Moon by a crust-breaching impact event. *Earth Planet. Sci. Lett.*
- 556 Bonifacie M., Jendrzewski N., Agrinier P., Humler E., Coleman M. and Javoy M. (2008) The
557 Chlorine Isotope Composition of Earth's Mantle. *Science (80-.)*. **319**, 1518–1520.
- 558 Bonnand P., Parkinson I. J. and Anand M. (2016) Mass dependent fractionation of stable chromium
559 isotopes in mare basalts: Implications for the formation and the differentiation of the Moon.
560 *Geochim. Cosmochim. Acta* **175**, 208–221.
- 561 Boyce J. W. and Hervig R. L. (2008) Magmatic degassing histories from apatite volatile stratigraphy.
562 *Geology* **36**, 63.
- 563 Boyce J. W., Liu Y., Rossman G. R., Guan Y., Eiler J. M., Stolper E. M. and Taylor L. A. (2010)
564 Lunar apatite with terrestrial volatile abundances. *Nature* **466**, 466–9.
- 565 Boyce J. W., Tomlinson S. M., McCubbin F. M., Greenwood J. P. and Treiman A. H. (2014) The
566 lunar apatite paradox. *Science* **344**, 400–2.
- 567 Boyce J. W., Treiman A. H., Guan Y., Ma C., Eiler J. M., Gross J., Greenwood J. P. and Stolper E. M.
568 (2015) The chlorine isotope fingerprint of the lunar magma ocean. *Sci. Adv.* **1**, 1–8.
- 569 Canup Robin M., Visscher Channon, Salmon Julien and Fegley Bruce (2015) Lunar volatile
570 depletion due to incomplete accretion within an impact-generated disk. *Am. Astron. Soc.*
- 571 Canup R. M. (2012) Forming a Moon with an Earth-like composition via a giant impact. *Science* **338**,
572 1052–5.
- 573 Charlier B. L. A., Nowell G. M., Parkinson I. J., Kelley S. P., Pearson D. G. and Burton K. W. (2012)
574 High temperature strontium stable isotope behaviour in the early solar system and planetary
575 bodies. *Earth Planet. Sci. Lett.* **329–330**, 31–40.
- 576 Compston W., Vernon M. J., Berry H., Rudowski R., Gray C. M. and Ware N. (1972) Apollo 14
577 mineral ages and the thermal history of the Fra Mauro formation. *Lunar Planet. Sci. Conf.* **3**,
578 1487–1501.
- 579 Compston W., Vernon M. J., Berry H., Rudowski R., Gray C. M., Ware N., Chappell B. W. and Kaye
580 M. (1972) Age and Petrogenesis of Apollo 14 Basalts. *Lunar Planet. Sci. Conf.* **3**.
- 581 Čuk M. and Stewart S. T. (2012) Making the Moon from a fast-spinning Earth: a giant impact
582 followed by resonant despinning. *Science* **338**, 1047–52.
- 583 Dasch E. ., Shih C.-Y., Bansal B. ., Wiesmann H. and Nyquist L. . (1987) Isotopic analysis of basaltic
584 fragments from lunar breccia 14321: Chronology and petrogenesis of pre-Imbrium mare

- 585 volcanism. *Geochim. Cosmochim. Acta* **51**, 3241–3254.
- 586 Dauphas N., Chen J. H. and Papanastassiou D. A. (2015) Testing Earth-Moon Isotopic
587 Homogenization with Calcium-48. *Lunar Planet. Sci. Conf.* **46**, 2436.
- 588 Day J. M. D., Moynier F. and Shearer C. K. (2017) Late-stage magmatic outgassing from a volatile-
589 depleted Moon. *Proc. Natl. Acad. Sci. U. S. A.* **114**, 9547–9551.
- 590 El Goresy A., Ramdohr P. and Taylor L. A. (1971) The geochemistry of the opaque minerals in
591 Apollo 14 crystalline rocks. *Earth Planet. Sci. Lett.* **13**, 121–129.
- 592 Elkins-Tanton L. T., Burgess S. and Yin Q.-Z. (2011) The lunar magma ocean : Reconciling the
593 solidification process with lunar petrology and geochronology. *Earth Planet. Sci. Lett.* **304**, 326–
594 336.
- 595 Fegley B. (1991) Thermodynamic models of the chemistry of lunar volcanic gases. *Geophys. Res.*
596 *Lett.* **18**, 2073–2076.
- 597 Fischer-Gödde M. and Becker H. (2012) Osmium isotope and highly siderophile element constraints
598 on ages and nature of meteoritic components in ancient lunar impact rocks. *Geochim.*
599 *Cosmochim. Acta* **77**, 135–156.
- 600 Gola A. A., D’Anna B., Feilberg K. L., Sellevåg S. R., Bache-Andreassen L. and Nielsen C. J. (2005)
601 Kinetic isotope effects in the gas phase reactions of OH and Cl with CH₃Cl, CD₃Cl,
602 and 13CHCl. *Atmos. Chem. Phys.* **5**, 2395–2402.
- 603 Gomes R., Levison H. F., Tsiganis K. and Morbidelli A. (2005) Origin of the cataclysmic Late Heavy
604 Bombardment period of the terrestrial planets. *Nature* **435**, 466–469.
- 605 Greenwood J. P., Itoh S., Sakamoto N., Warren P., Taylor L. and Yurimoto H. (2011) Hydrogen
606 isotope ratios in lunar rocks indicate delivery of cometary water to the Moon. *Nat. Geosci.* **4**,
607 79–82.
- 608 Hauri E. H., Saal A. E., Rutherford M. J. and Van Orman J. A. (2015) Water in the Moon’s interior:
609 Truth and consequences. *Earth Planet. Sci. Lett.* **409**, 252–264.
- 610 Herwartz D., Pack A., Friedrichs B. and Bischoff A. (2014) Identification of the giant impactor Theia
611 in lunar rocks. *Science* **344**, 1146–50.
- 612 Herzog G. F., Moynier F., Albarède F. and Berezhnoy A. A. (2009) Isotopic and elemental
613 abundances of copper and zinc in lunar samples, Zagami, Pele’s hairs, and a terrestrial basalt.
614 *Geochim. Cosmochim. Acta* **73**, 5884–5904.
- 615 Hiesinger H. and Head J. W. (2006) New Views of Lunar Geoscience: An Introduction and Overview.
616 *Rev. Mineral. Geochemistry* **60**, 1–81.
- 617 Huang L., Sturchio N. ., Abrajano T., Heraty L. . and Holt B. . (1999) Carbon and chlorine isotope
618 fractionation of chlorinated aliphatic hydrocarbons by evaporation. *Org. Geochem.* **30**, 777–785.
- 619 Hui H., Neal C. R., Shih C.-Y. and Nyquist L. E. (2013) Petrogenetic association of the oldest lunar
620 basalts: Combined Rb–Sr isotopic and trace element constraints. *Earth Planet. Sci. Lett.* **373**,
621 150–159.
- 622 Hui H., Oshrin J. G. and Neal C. R. (2011) Investigation into the petrogenesis of Apollo 14 high-Al
623 basaltic melts through crystal stratigraphy of plagioclase. *Geochim. Cosmochim. Acta* **75**, 6439–
624 6460.
- 625 Husain L., Sutter J. F. and Schaeffer O. A. (1971) Ages of crystalline rocks from fra Mauro. *Science*

- 626 **173**, 1235–6.
- 627 Kato C., Moynier F., Valdes M. C., Dhaliwal J. K. and Day J. M. D. (2015) Extensive volatile loss
628 during formation and differentiation of the Moon. *Nat. Commun.* **6**, 7617.
- 629 Kaufmann R., Long A., Bentley H. and Davis S. (1984) Natural chlorine isotope variations. *Nature*
630 **309**, 338–340.
- 631 Konecke B. A., Fiege A., Simon A. C. and Holtz F. (2017) Cryptic metasomatism during late-stage
632 lunar magmatism implicated by sulfur in apatite. *Geology* **45**, G39249.1.
- 633 Krähenbühl U., Ganapathy R., Morgan J. W. and Anders E. (1973) Volatile elements in Apollo 16
634 samples: Implications for highland volcanism and accretion history of the moon. *Lunar Planet.*
635 *Sci. Conf.* **4**, 1325.
- 636 Kusebauch C., John T., Whitehouse M. J., Klemme S. and Putnis A. (2015) Distribution of halogens
637 between fluid and apatite during fluid-mediated replacement processes. *Geochim. Cosmochim.*
638 *Acta* **170**, 225–246.
- 639 Liebscher A., Barnes J. and Sharp Z. (2006) Chlorine isotope vapor–liquid fractionation during
640 experimental fluid-phase separation at 400 °C/23 MPa to 450 °C/42 MPa. *Chem. Geol.* **234**,
641 340–345.
- 642 Lugmair G. W. and Shukolyukov A. (1998) Early solar system timescales according to ⁵³Mn–⁵³Cr
643 systematics. *Geochim. Cosmochim. Acta* **62**, 2863–2886.
- 644 Mark R. K., Lee-Hu C.-N. and Weatherill G. W. (1974) Rb–Sr age of lunar igneous rocks 62295 and
645 14310. *Geochim. Cosmochim. Acta* **38**, 1643–1648.
- 646 McCubbin F. M., Jolliff B. L., Nekvasil H., Carpenter P. K., Zeigler R. a., Steele A., Elardo S. M. and
647 Lindsley D. H. (2011) Fluorine and chlorine abundances in lunar apatite: Implications for
648 heterogeneous distributions of magmatic volatiles in the lunar interior. *Geochim. Cosmochim.*
649 *Acta* **75**, 5073–5093.
- 650 McCubbin F. M., Vander Kaaden K. E., Tartèse R., Boyce J. W., Mikhail S., Whitson E. S., Bell A.
651 S., Anand M., Franchi I. A., Wang J. and Hauri E. H. (2015) Experimental investigation of F,
652 Cl, and OH partitioning between apatite and Fe-rich basaltic melt at 1.0 to 1.2 GPa and 950 to
653 1000 °C. *Am. Mineral.* **100**, 1790–1802.
- 654 McCubbin F. M., Vander Kaaden K. E., Tartèse R., Klima R. L., Liu Y., Mortimer J., Barnes J. J.,
655 Shearer C. K., Treiman A. H., Lawrence D. J., Elardo S. M., Hurley D. M., Boyce J. W. and
656 Anand M. (2015) Magmatic volatiles (H, C, N, F, S, Cl) in the lunar mantle, crust, and regolith:
657 Abundances, distributions, processes, and reservoirs. *Am. Mineral.* **100**, 1668–1707.
- 658 McCubbin F. M., Steele A., Hauri E. H., Nekvasil H., Yamashita S. and Hemley R. J. (2010)
659 Nominally hydrous magmatism on the Moon. *Proc. Natl. Acad. Sci. U. S. A.* **107**, 11223–8.
- 660 McCubbin F. M., Steele A., Nekvasil H., Schnieders A., Rose T., Fries M., Carpenter P. K. and Jolliff
661 B. L. (2010) Detection of structurally bound hydroxyl in fluorapatite from Apollo Mare basalt
662 15058,128 using TOF-SIMS. *Am. Mineral.* **95**, 1141–1150.
- 663 McKay D. S., Clanton U. S., Heiken G. H., Morrison D. A., Taylor R. M. and Ladle G. (1972) Vapor
664 Phase Crystallization in Apollo 14 Breccias and Size Analysis of Apollo 14 Soils. *Lunar Planet.*
665 *Sci. Conf.* **3**, 529.
- 666 McKay G. A., McKay G. A., Wiesmann H., Bansal B. M. and Shih C.-Y. (1979) Petrology,
667 chemistry, and chronology of Apollo 14 KREEP basalts. *Lunar Planet. Sci. Conf.* **10**, 181–205.

- 668 Meyer C., Williams I. S. and Compston W. (1996) Uranium-lead ages for lunar zircons: Evidence for
669 a prolonged period of granophyre formation from 4.32 to 3.88 Ga. *Meteorit. Planet. Sci.* **31**,
670 370–387.
- 671 Morbidelli A., Marchi S., Bottke W. F. and Kring D. A. (2012) A sawtooth-like timeline for the first
672 billion years of lunar bombardment. *Earth Planet. Sci. Lett.* **355**, 144–151.
- 673 Neal C. R. and Kramer G. Y. (2006) The petrogenesis of the Apollo 14 high-Al mare basalts. *Am.*
674 *Mineral.* **91**, 1521–1535.
- 675 Neal C. R. and Taylor L. A. (1989) Metasomatic products of the lunar magma ocean: The role of
676 KREEP dissemination. *Geochim. Cosmochim. Acta* **53**, 529–541.
- 677 Neal C. R., Taylor L. A. and Lindstrom M. M. (1988) Apollo 14 mare basalt petrogenesis -
678 Assimilation of KREEP-like components by a fractionating magma. *Lunar Planet. Sci. Conf.* **18**,
679 139–153.
- 680 Neal C. R., Taylor L. A., Schmitt R. A., Hughes S. S. and Lindstrom M. M. (1989) High alumina
681 (HA) and very high potassium (VHK) basalt clasts from Apollo 14 breccias. II - Whole rock
682 geochemistry - Further evidence for combined assimilation and fractional crystallization within
683 the lunar crust. *Lunar Planet. Sci. Conf.* **19**, 147–161.
- 684 Nemchin A. A., Pidgeon R. T., Healy D., Grange M. L., Whitehouse M. J. and Vaughan J. (2009) The
685 comparative behavior of apatite-zircon U-Pb systems in Apollo 14 breccias: Implications for the
686 thermal history of the Fra Mauro Formation. *Meteorit. Planet. Sci.* **44**, 1717–1734.
- 687 Nemchin A. A., Pidgeon R. T., Whitehouse M. J., Vaughan J. P. and Meyer C. (2008) SIMS U-Pb
688 study of zircon from Apollo 14 and 17 breccias: Implications for the evolution of lunar KREEP.
689 *Geochim. Cosmochim. Acta* **72**, 668–689.
- 690 Nemchin A., Grange M. and Pidgeon R. (2010) Distribution of rare earth elements in lunar zircon.
691 *Am. Astron. Soc.* **95**, 273–283.
- 692 Norman M. D., Duncan R. A. and Huard J. J. (2006) Identifying impact events within the lunar
693 cataclysm from ^{40}Ar - ^{39}Ar ages and compositions of Apollo 16 impact melt rocks. *Geochim.*
694 *Cosmochim. Acta* **70**, 6032–6049.
- 695 Nunes P. D. and Tatsumoto M. (1973) Excess lead in rusty rock 66095 and implications for an early
696 lunar differentiation. *Science* **182**, 916–20.
- 697 Paniello R. C., Day J. M. D. and Moynier F. (2012) Zinc isotopic evidence for the origin of the Moon.
698 *Nature* **490**, 376–9.
- 699 Papanastassiou D. A. and Wasserburg G. J. (1971) RbSr ages of igneous rocks from the Apollo 14
700 mission and the age of the Fra Mauro formation. *Earth Planet. Sci. Lett.* **12**, 36–48.
- 701 Patiño Douce A. E. and Roden M. (2006) Apatite as a probe of halogen and water fugacities in the
702 terrestrial planets. *Geochim. Cosmochim. Acta* **70**, 3173–3196.
- 703 Richet P., Bottinga Y. and Javoy M. (1977) A review of hydrogen, carbon, nitrogen, oxygen, sulphur,
704 and chlorine stable isotope fractionation among gaseous molecules. *Annu. Rev. Earth Planet.*
705 *Sci.* **5**, 65–110.
- 706 Ridley W. I. (1975) On high-alumina mare basalts. *Lunar Sci. Conf.* **6**, 131–145.
- 707 Robinson K. L., Barnes J. J., Nagashima K., Thomen A., Franchi I. A., Huss G. R., Anand M. and
708 Taylor G. J. (2016) Water in evolved lunar rocks: Evidence for multiple reservoirs. *Geochim.*
709 *Cosmochim. Acta* **188**, 244–260.

- 710 Rubie D. C., Jacobson S. a., Morbidelli a., O'Brien D. P., Young E. D., de Vries J., Nimmo F., Palme
711 H. and Frost D. J. (2015) Accretion and differentiation of the terrestrial planets with implications
712 for the compositions of early-formed Solar System bodies and accretion of water. *Icarus* **248**,
713 89–108.
- 714 Saal A. E., Hauri E. H., Van Orman J. a and Rutherford M. J. (2013) Hydrogen isotopes in lunar
715 volcanic glasses and melt inclusions reveal a carbonaceous chondrite heritage. *Science* **340**,
716 1317–20.
- 717 Schauble E. A., Rossman G. R., Taylor, H. P. J. and Taylor H. . (2003) Theoretical estimates of
718 equilibrium chlorine-isotope fractionations. *Geochim. Cosmochim. Acta* **67**, 3267–3281.
- 719 Schönbächler M., Lee D.-C., Rehkämper M., Halliday A. N., Fehr M. A., Hattendorf B. and Günther
720 D. (2003) Zirconium isotope evidence for incomplete admixing of r-process components in the
721 solar nebula. *Earth Planet. Sci. Lett.* **216**, 467–481.
- 722 Schonfeld E. and Meyer, Charles J. (1972) The abundances of components of the lunar soils by a
723 least-squares mixing model and the formation age of KREEP. *Lunar Planet. Sci. Conf.* **3**, 1397.
- 724 Sharp Z., Barnes J., Fischer T. and Halick M. (2010) An experimental determination of chlorine
725 isotope fractionation in acid systems and applications to volcanic fumaroles. *Geochim.*
726 *Cosmochim. Acta* **74**, 264–273.
- 727 Sharp Z. D., Barnes J. D., Brearley A. J., Chaussidon M., Fischer T. P. and Kamenetsky V. S. (2007)
728 Chlorine isotope homogeneity of the mantle, crust and carbonaceous chondrites. *Nature* **446**,
729 1062–5.
- 730 Sharp Z. D. D., Mercer J. A. A., Jones R. H. H., Brearley A. J. J., Selverstone J., Bekker A. and
731 Stachel T. (2013) The Chlorine Isotope Composition of Chondrites and Earth. *Geochim.*
732 *Cosmochim. Acta* **107**, 189–204.
- 733 Sharp Z. D., Shearer C. K., McKeegan K. D., Barnes J. D. and Wang Y. Q. (2010) The chlorine
734 isotope composition of the moon and implications for an anhydrous mantle. *Science* **329**, 1050–
735 3.
- 736 Shearer C. K., Hess P. C., Wieczorek M. A., Pritchard M. E., Parmentier E. M., Borg L. E., Longhi J.,
737 Elkins-Tanton L. T., Neal C. R., Antonenko I., Canup R. M., Halliday A. N., Grove T. L., Hager
738 B. H., Lee D.-C. and Wiechert U. (2006) Thermal and Magmatic Evolution of the Moon. *Rev.*
739 *Mineral. Geochemistry* **60**, 365–518.
- 740 Shearer C. K., Sharp Z. D., Burger P. V., McCubbin F. M., Provencio P. P., Brearley A. J. and Steele
741 A. (2014) Chlorine distribution and its isotopic composition in “rusty rock” 66095. Implications
742 for volatile element enrichments of “rusty rock” and lunar soils, origin of “rusty” alteration, and
743 volatile element behavior on the Moon. *Geochim. Cosmochim. Acta* **139**, 411–433.
- 744 Shinohara H. (2009) A missing link between volcanic degassing and experimental studies on chloride
745 partitioning. *Chem. Geol.* **263**, 51–59.
- 746 Snape J. F., Nemchin A. A., Bellucci J. J. and Whitehouse M. J. (2017) Pb isotopes in the impact melt
747 breccia 66095: Association with the Imbrium basin and the isotopic composition of lithologies at
748 the Apollo 16 landing site. *Chem. Geol.* **466**, 608–616.
- 749 Snape J. F., Nemchin A. A., Grange M. L., Bellucci J. J., Thiessen F. and Whitehouse M. J. (2016)
750 Phosphate ages in Apollo 14 breccias: Resolving multiple impact events with high precision U–
751 Pb SIMS analyses. *Geochim. Cosmochim. Acta* **174**, 13–29.
- 752 Snyder G. A., Borg L. E., Nyquist L. E. and Taylor L. A. (2000) Chronology and Isotopic Constraints
753 on Lunar Evolution. In *Origin of the earth and moon* (eds. R. M. Canup and K. Righter).

- 754 Tucson: University of Arizona Press. pp. 361–395.
- 755 Stöffler D. and Ryder G. (2001) Stratigraphy and Isotope Ages of Lunar Geologic Units:
756 Chronological Standard for the Inner Solar System. *Space Sci. Rev.* **96**, 9–54.
- 757 Tartèse R., Anand M., Barnes J. J., Starkey N. A., Franchi I. A. and Sano Y. (2013) The abundance,
758 distribution, and isotopic composition of Hydrogen in the Moon as revealed by basaltic lunar
759 samples: Implications for the volatile inventory of the Moon. *Geochim. Cosmochim. Acta* **122**,
760 58–74.
- 761 Tartèse R., Anand M., Joy K. H. and Franchi I. A. (2014) H and Cl isotope systematics of apatite in
762 brecciated lunar meteorites Northwest Africa 4472, Northwest Africa 773, Sayh al Uhaymir 169,
763 and Kalahari 009. *Meteorit. Planet. Sci.* **49**, 2266–2289.
- 764 Tartèse R., Anand M., McCubbin F. M., Elardo S. M., Shearer C. K. and Franchi I. A. (2014) Apatites
765 in lunar KREEP basalts: The missing link to understanding the H isotope systematics of the
766 Moon. *Geology* **42**, 363–366.
- 767 Tartèse R., Anand M., McCubbin F. M., Elardo S. M., Shearer C. K. and Franchi I. A. (2014) Apatites
768 in lunar KREEP basalts: The missing link to understanding the H isotope systematics of the
769 Moon. *Geology* **42**, 363–366.
- 770 Tatsumoto M., Hedge C. E., Doe B. R. and Unruh D. M. (1972) U-Th-Pb and Rb-Sr measurements on
771 some Apollo 14 lunar samples. *Lunar Planet. Sci. Conf.* **3**, 1531.
- 772 Taylor L. A., Patchen A., Mayne R. G. and Taylor D.-H. (2004) The most reduced rock from the
773 moon , Apollo 14 basalt 14053 : Its unique features and their origin. *Am. Mineral.* **89**, 1617–
774 1624.
- 775 Tera F., Papanastassiou D. A. and Wasserburg G. J. (1974) Isotopic evidence for a terminal lunar
776 cataclysm. *Earth Planet. Sci. Lett.* **22**, 1–21.
- 777 Treiman A. H., Boyce J. W., Gross J., Guan Y., Eiler J. M. and Stolper E. M. (2014) Phosphate-
778 halogen metasomatism of lunar granulite 79215: Impact-induced fractionation of volatiles and
779 incompatible elements. *Am. Mineral.* **99**, 1860–1870.
- 780 Turner G., Huneke J. C., Podosek F. A. and Wasserburg G. J. (1971) ⁴⁰Ar-³⁹Ar ages and cosmic ray
781 exposure ages of Apollo 14 samples. *Earth Planet. Sci. Lett.* **12**, 19–35.
- 782 Turner G., Huneke J. C., Podosek F. A. and Wasserburg G. J. (1972) Ar⁴⁰-Ar³⁰ systematics in rocks
783 and separated minerals from Apollo 14. *Lunar Planet. Sci. Conf.* **3**, 1589–1612.
- 784 Ustunisik G., Nekvasil H. and Lindsley D. (2011) Differential degassing of H₂O, Cl, F, and S:
785 Potential effects on lunar apatite. *Am. Mineral.* **96**, 1650–1653.
- 786 Ustunisik G., Nekvasil H., Lindsley D. H. and McCubbin F. M. (2015) Degassing pathways of Cl-, F-
787 , H-, and S-bearing magmas near the lunar surface: Implications for the composition and Cl
788 isotopic values of lunar apatite. *Am. Mineral.* **100**, 1717–1727.
- 789 Valdes M. C., Moreira M., Foriel J. and Moynier F. (2014) The nature of Earth's building blocks as
790 revealed by calcium isotopes. *Earth Planet. Sci. Lett.* **394**, 135–145.
- 791 Wang K. and Jacobsen S. B. (2016) Potassium isotopic evidence for a high-energy giant impact origin
792 of the Moon. *Nature* **538**, 487–490.
- 793 Warren P. H. and Wasson J. T. (1979) The origin of KREEP. *Rev. Geophys.* **17**, 73.
- 794 Webster J. D., Kinzler R. J. and Mathez E. A. (1999) Chloride and water solubility in basalt and

- 795 andesite melts and implications for magmatic degassing. *Geochim. Cosmochim. Acta* **63**, 729–
796 738.
- 797 Webster J. D., Tappen C. M. and Mandeville C. W. (2009) Partitioning behavior of chlorine and
798 fluorine in the system apatite–melt–fluid. II: Felsic silicate systems at 200MPa. *Geochim.*
799 *Cosmochim. Acta* **73**, 559–581.
- 800 Wetzel D. T., Hauri E. H., Saal A. E. and Rutherford M. J. (2015) Carbon content and degassing
801 history of the lunar volcanic glasses. *Nat. Geosci.* **8**, 755–758.
- 802 Wiechert U., Halliday A. N., Lee D. C., Snyder G. A., Taylor L. A. and Rumble D. (2001) Oxygen
803 isotopes and the moon-forming giant impact. *Science* **294**, 345–8.
- 804 Wieczorek M. A., Neumann G. A., Nimmo F., Kiefer W. S., Taylor G. J., Melosh H. J., Phillips R. J.,
805 Solomon S. C., Andrews-Hanna J. C., Asmar S. W., Konopliv A. S., Lemoine F. G., Smith D.
806 E., Watkins M. M., Williams J. G. and Zuber M. T. (2013) The crust of the Moon as seen by
807 GRAIL. *Science* **339**, 671–5.
- 808 Wilhelms D. E., McCauley J. F. with sections by and Trask N. J. (1987) *The geologic history of the*
809 *Moon.*,
- 810 York D., Kenyon W. J. and Doyle R. J. (1972) ⁴⁰Ar-³⁹Ar ages of Apollo 14 and 15 samples. *Lunar*
811 *Planet. Sci. Conf.* **3**, 1613.
- 812 Young E. D., Kohl I. E., Warren P. H., Rubie D. C., Jacobson S. A. and Morbidelli A. (2016) Oxygen
813 isotopic evidence for vigorous mixing during the Moon-forming giant impact. *Science* (80-.).
814 **351**, 493–496.
- 815 Zambardi T., Poitrasson F., Corgne A., Méheut M., Quitté G. and Anand M. (2013) Silicon isotope
816 variations in the inner solar system: Implications for planetary formation, differentiation and
817 composition. *Geochim. Cosmochim. Acta* **121**, 67–83.
- 818 Zhang J., Dauphas N., Davis A. M., Leya I. and Fedkin A. (2012) The proto-Earth as a significant
819 source of lunar material. *Nat. Geosci.* **5**, 251–255.
- 820

Figure Captions

Figure 1: Ternary diagram of apatite X-site occupancy (mol%), assuming that X-site is completely filled with F + Cl + H₂O. F was calculated by difference for all analyses except those with F abundances reported in Table 3. Literature data from McCubbin et al., (2015), and references therein.

Figure 2: $\delta^{37}\text{Cl}$ data for volcanic samples (see text) 14053, 14072, and 14321,1482 plotted against (A) Cl and (B) H₂O abundances, and for impact melt samples (see text) 14073 and 14310 plotted against (C) Cl concentration (D) H₂O abundances.

Figure 3: All available $\delta^{37}\text{Cl}$ data plotted against (A) H₂O (ppm), and (B) Cl (ppm) with fields for literature data.. Literature data from Barnes et al. (2016), Boyce et al. (2015), Tartèse et al. (2014a), Treiman et al. (2014), and Sharp et al. (2010). NWA refers to KREEP-rich clast in NWA4472 from Tartèse et al. (2014b). Note the difference in VHK and granulite fields between A and B result from the highest $\delta^{37}\text{Cl}$ values for each rock type not having H₂O abundance associated with them.

Figure 4: All available $\delta^{37}\text{Cl}$ data for Apollo samples plotted against bulk rock La/Lu. La and Lu abundances averaged from data taken from Lunar Sample Compendium. References are given in SM1 Table 1. Literature data from Barnes et al. (2016), Boyce et al. (2015), Treiman et al. (2014), and Sharp et al. (2010). '14321' refers to 14321,1482.

Figure 5: F abundance of apatite (wt.%) plotted against $\delta^{37}\text{Cl}$ values for samples in this study. F contents are those either measured (see Table 2) or calculated by difference assuming the X-site is completely filled with F + Cl + H₂O. '14321' refers to 14321,1482.

Figure 6: Schematic diagram of vapor-release metasomatism following impact-events or emplacement of lava flows. After an impact-event or volcanic eruption, a hot zone (~1000 °C) develops underneath the ejecta blanket/lava flow. As crystallization occurs in this hot zone, vapors are released. These vapors travel up through the solidifying ejector blanket/lava flow allowing for vapor interaction with warmed-up/solidifying rock. Cartoon after Shearer et al. (2014) and McKay et al. (1972).

Figure 1

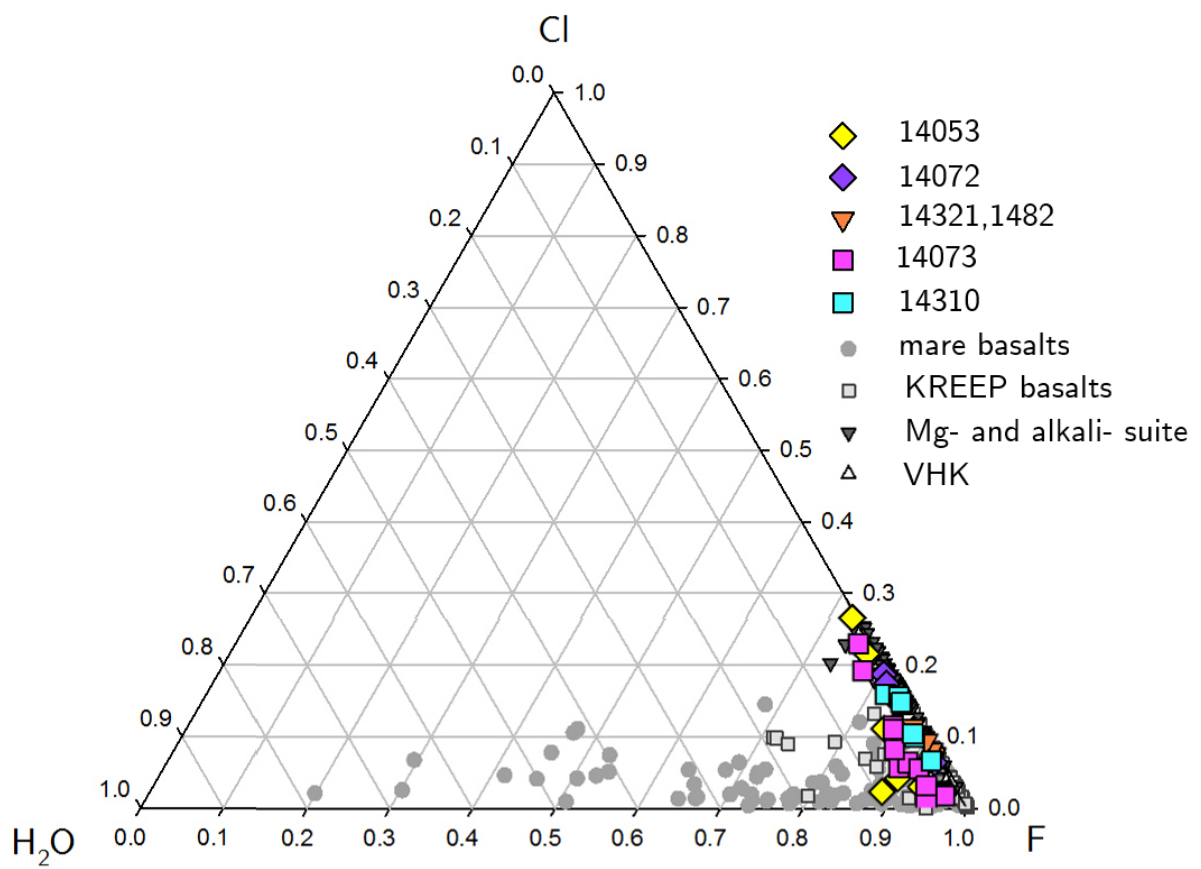


Figure 2

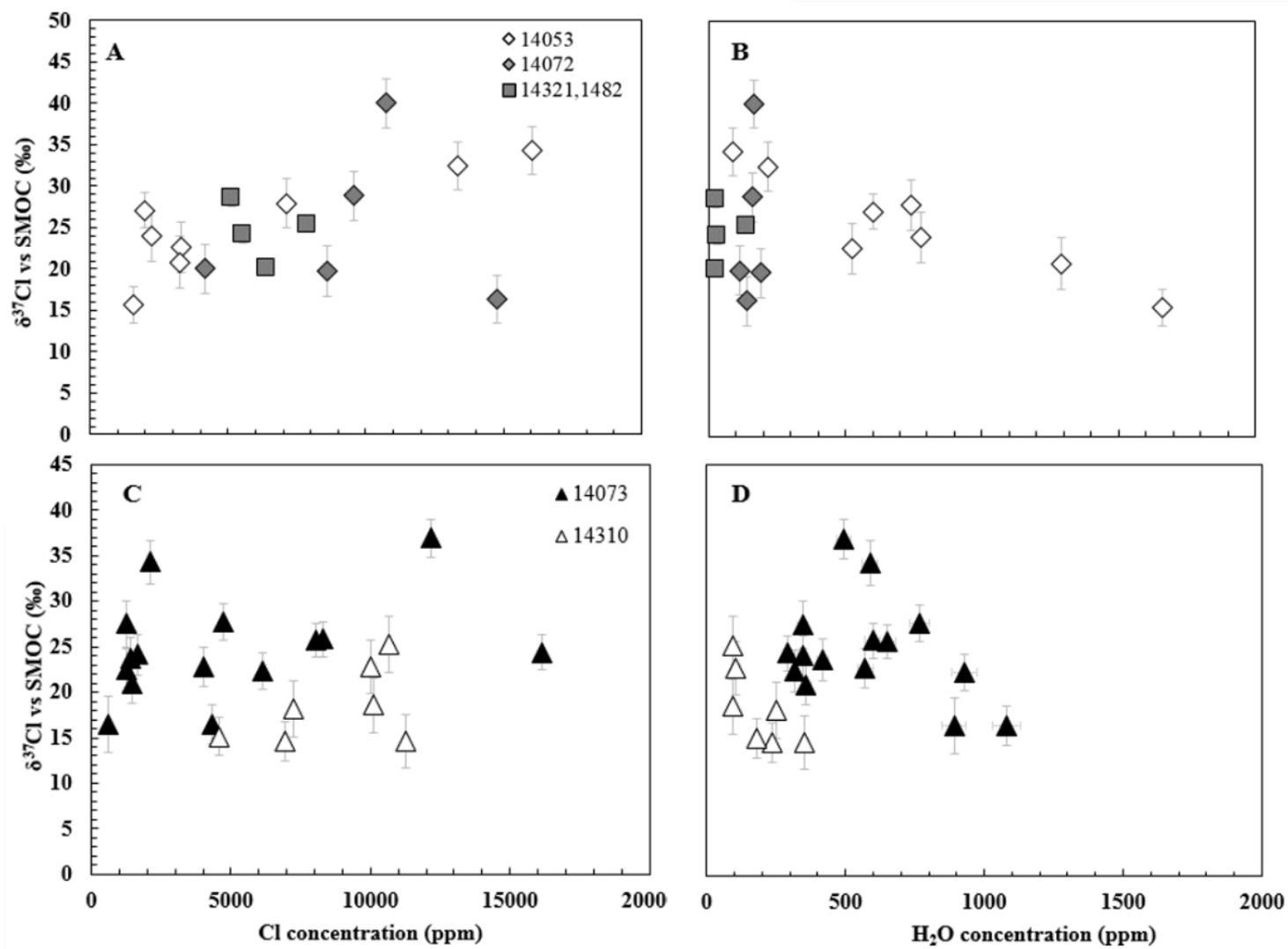


Figure 3

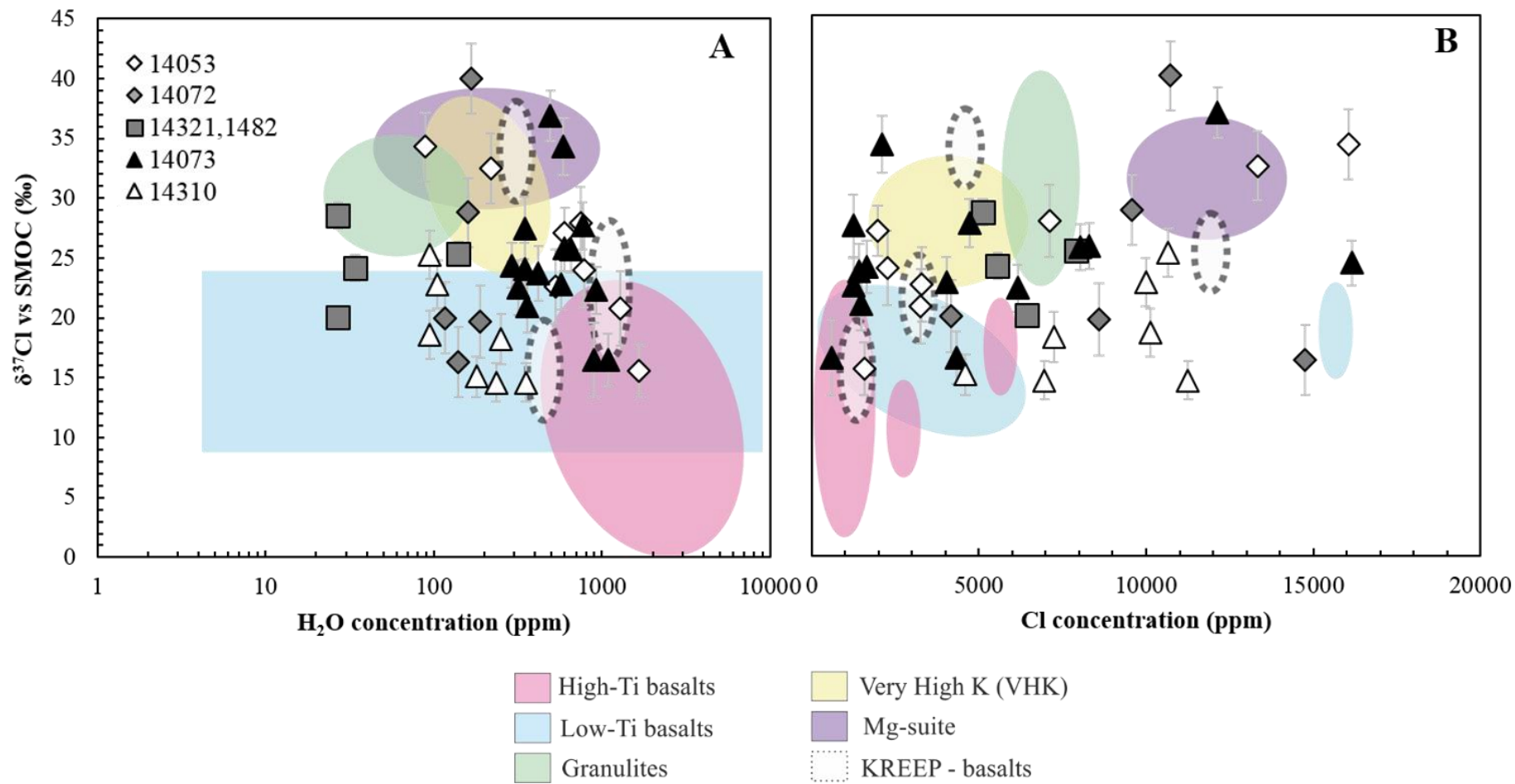


Figure 4

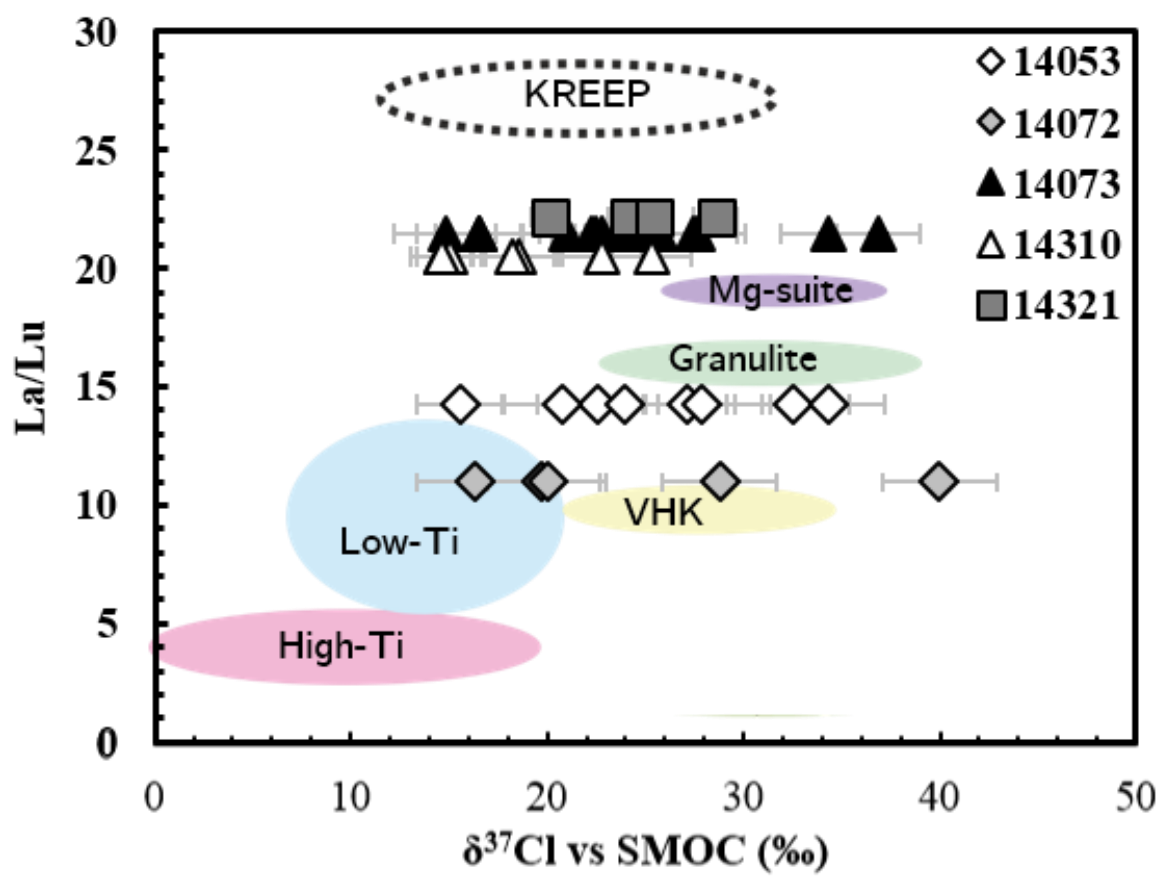


Figure 5

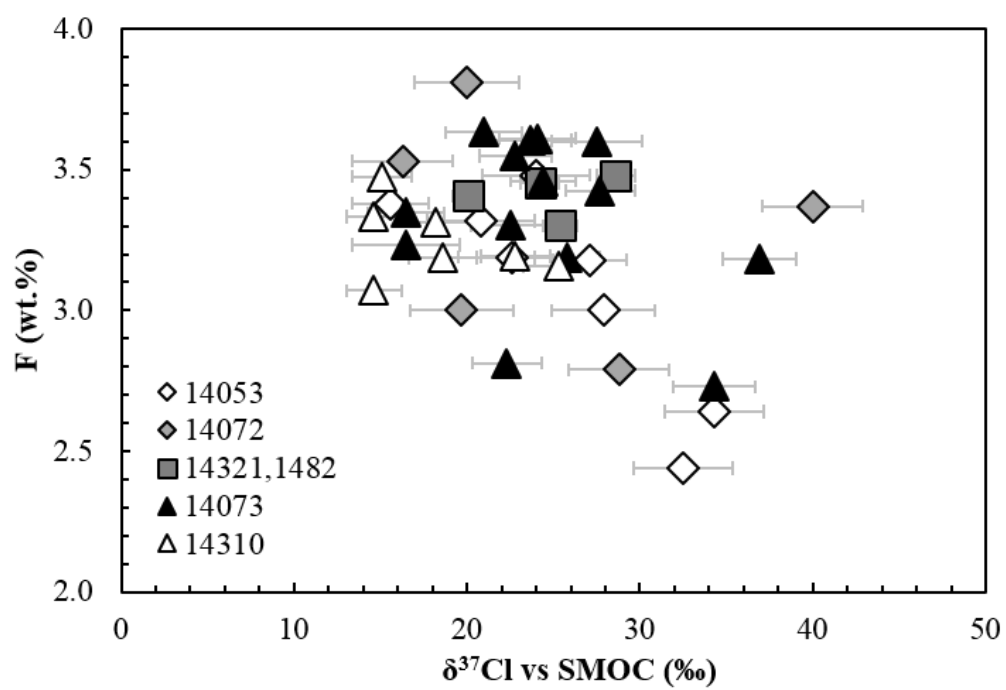


Figure 6

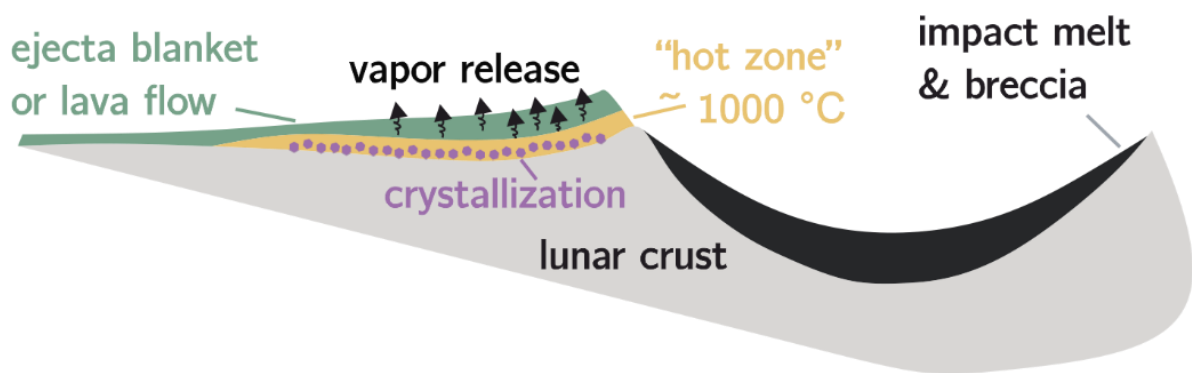


Table 1: Radiometric dates obtained for Apollo 14 samples studied here and their geochemical grouping. All dates are in Ga. Data from a) Husain et al. (1971), b) Papanastassiou and Wasserburg (1971), c) York et al. (1972), d) Compston et al. (1972b), e) Dasch et al. (1987), f) Turner et al. (1972), g) Mark et al. (1974), and h) Tatsumoto et al. (1972). *Rb-Sr data re-processed with updated decay constant, all dates from Hui et al. (2013). **14072 does not belong to any group of high-Al basalts but is geochemically intermediate between Group A and C. Note a crystallization age of 3905 ± 8 Ma has also been determined for 14072 from Pb/Pb dating by Snape et al. (2016).

	Ages			Geochemical Features	
	$^{40}\text{Ar}/^{39}\text{Ar}$	Rb-Sr	Rb-Sr*	Group	Crystallization
14053	3.92 ± 0.08^a	3.96 ± 0.04^b	3.94 ± 0.03	C	open
14072	4.04 ± 0.05^c	3.99 ± 0.09^d	3.98 ± 0.15 3.98 ± 0.09	A – C**	open
14321,1482				B	open
14073	3.88 ± 0.05^e	3.88 ± 0.04^a	3.86 ± 0.02	impact melt	closed
14310	3.88 ± 0.05^f	3.94 ± 0.03^g 3.84 ± 0.04^h	3.85 ± 0.02 3.92 ± 0.06 3.90 ± 0.19	impact melt	closed

Table 2: Measured Cl isotopic values (‰), and background corrected Cl (ppm), H₂O (ppm), and F (wt.%) abundances of apatite in the Apollo 14 samples analyzed in this study. (B) and (C) refer to Fig.2 panel for 14072,13.

Sample	$\delta^{37}\text{Cl}$ (‰)	2 σ (‰)	Cl (ppm)	2 σ (ppm)	H ₂ O (ppm)	2 σ (ppm)	F (wt.%)	2 σ (‰)
<i>Sample 14053,19</i>								
14053_A1_Ap#1	15.6	2.2	1569	2	1662	80	3.38	0.04
14053_A1_Ap#2	27.1	2.1	1967	2	601	29	3.18	0.03
14053_A4_Ap#4a	34.3	2.9	16054	17	89	4.3	2.64	0.03
14053_A4_Ap#4b	32.5	2.9	13332	14	218	11	2.44	0.03
14053_A5_Ap#5a	22.6	3.1	3292	4	526	25	3.19	0.03
14053_A5_Ap#5b	27.9	3.0	7109	8	743	36	3.00	0.03
14053_A8_Ap#8a	24.0	3.1	2251	3	779	38		
14053_A8_Ap#8b	20.8	3.1	3263	4	1292	62		
<i>Sample 14072,13</i>								
14072_A7_Ap#3	19.7	3.0	8589	10	189	9	3.00	0.03
14072_A3_Ap#1(B)	16.3	2.9	14759	15	140	7	3.53	0.04
14072_A3_Ap#1(C)	20.0	3.0	4167	5	117	6		
14072_A4_Ap#1	40.0	2.9	10737	12	167	8	3.37	0.04
14072_A6_Ap#1	28.8	2.9	9580	11	160	8	2.79	0.03
<i>Sample 14321,1482</i>								
14321,1482_A3_Ap1a	28.6	1.1	5117	9	27	1		
14321,1482_A3_Ap1b	24.2	1.1	5549	10	34	1		
14321,1482_A4_Ap1a	25.4	1.0	7897	14	140	5		
14321,1482_A5_Ap2a	20.1	0.9	6414	10	27	1		
<i>Sample 14073,9</i>								
14073_A11_Ap#1	27.5	2.6	1241	2	346	17	3.04	0.03
14073_A11_Ap#2	23.7	2.3	1421	2	419	20		
14073_A11_Ap#3	24.1	2.2	1648	2	346	17		
14073_A11_Ap#4	21.0	2.2	1479	2	360	17		
14073_A11_Ap#5	22.5	2.3	1254	2	317	15		
14073_A12_Ap#a	16.5	2.2	4317	5	1081	52		
14073_A12_Ap#b	27.7	2.0	4713	5	766	37		
14073_A12_Ap#c	22.8	2.1	4021	5	572	28		
14073_A12_Ap#d	16.5	3.1	580	1	893	43		
14073_A17_Ap#a	22.3	2.0	6157	7	929	45		
14073_A17_Ap#b	24.4	1.9	16149	18	291	14		
14073_A18_Ap#a	34.3	2.4	2097	3	588	28	3.46	0.04
14073_A19_Ap#a	36.9	2.1	12146	13	493	24	2.73	0.03
14073_A19_Ap#b	25.8	1.9	8311	9	598	29		
14073_A19_Ap#c	25.7	1.9	8033	8	649	31		
<i>Sample 14310,171</i>								
14310_A1_Ap#1	14.6	1.6	6962	12	243	8		
14310_A1_Ap#2	15.1	1.7	4597	8	179	6		
14310_A2_Ap#1a	14.6	1.6	11256	19	354	11		
14310_A2_Ap#1b	22.8	2.0	9992	18	105	4		

14310_A2_Ap#1c	25.3	2.0	10654	19	95	3
14310_A2_Ap#2	18.6	2.0	10121	19	95	3
14310_A5_Ap#1	18.2	2.1	7238	13	251	8
